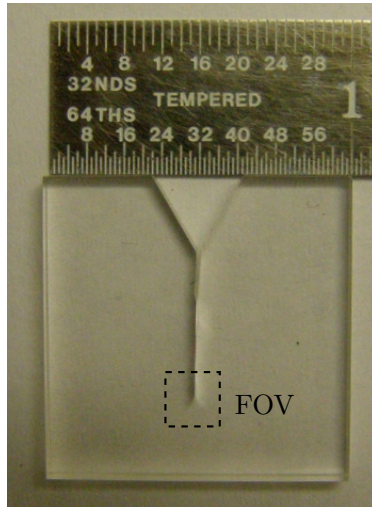
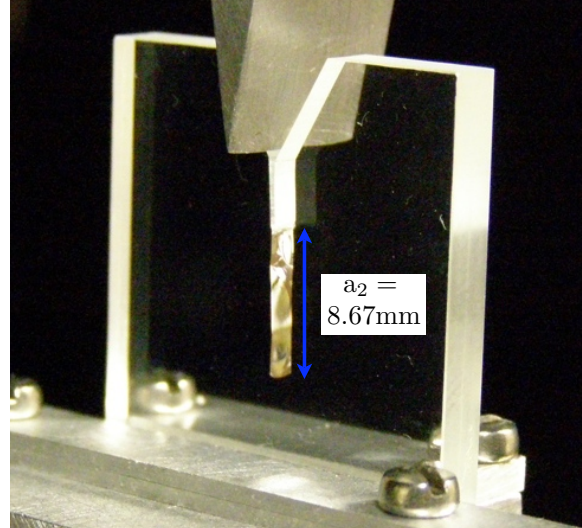


4.2.6 Crack with $K_I = 0.145 \text{ MPa}\sqrt{\text{m}}$ and $K_{II} = 0.63 \text{ kPa}\sqrt{\text{m}}$

This specimen, called HomC2, is made of Homalite-100, but this specimen has thickness of $h = 3.43$ mm, outer dimensions $25.46 \text{ mm} \times 25.46 \text{ mm}$, V-notch depth of 6.25 mm , straight notch length of $a_1 = 3.53 \text{ mm}$ and crack length of $s_2 = 8.67 \text{ mm}$. The optical field of view imaged onto the sensor is $4.57 \text{ mm} \times 4.57 \text{ mm}$, and the image resolution is $4.57 \mu\text{m}$. For this CGS setup, the Ronchi grating pitch, p , is $1 \text{ mm}/40$; the grating separation, $\tilde{\Delta}$, is 8.84 mm ; the wavelength of light from the linearly polarized HeNe laser is 632.8 nm ; and the resulting lateral shearing distance, d_{shear} , is $224 \mu\text{m}$. Figure 4.46(a) shows the specimen before loading with the experimental field of view indicated on the specimen. Figure 4.46(a) shows the specimen in the load apparatus prior to loading; the angled view of the specimen shows a very slight curvature to the crack tip through the thickness. The image is from taken looking towards the light source. The measured stress intensity values are $K_I = 0.145 \text{ MPa}\sqrt{\text{m}}$ and $K_{II} = 0.63 \text{ kPa}\sqrt{\text{m}}$, which give a mode-mixity ratio of $\mu_{SIF} = 0.0043$. This load case has the lowest recorded K_I for cracks in Homalite-100 during this study.



(a) Specimen with marked FOV



(b) Specimen with marked a_2

Figure 4.46: Specimen HomC2 before loading: (a) the small FOV is indicated; (b) the specimen is in the loading apparatus with the crack length a_2 indicated

Figures 4.47–4.49 present the photoelasticity and the vertical and horizontal shear CGS images. The fringe densities in these images are small due to the small K_I and K_{II} . These images have

similar fringe density as the $K_I = 0.259 \text{ MPa}\sqrt{\text{m}}$ case in specimen HomC1 even with a smaller K_I because specimen HomC2 is 56% thicker than specimen HomC1, meaning the two interferometric methods that scale by the specimen thickness can report similar fringe density for different loads. To reduce the noise source of the weak Fizeau fringes from the interference of the reflected light from the surfaces of the specimen, a Wiener filter with window size of $[25 \times 25]$ pixels is used on the photoelastic images before processing the data. In the images, a small dark ring is apparent on the crack plane about $250 \mu\text{m}$ behind the crack tip; this ring is a second crack tip at one of the surfaces of the specimen. As noted in Figure 4.46(b), the crack tip is not perfectly straight through the thickness. The curvature does not appear to affect the shape of the interference patterns except for blurring the data in the immediate vicinity of this back surface crack tip. Close observation of the crack tip shape in Figure 4.46(b) shows that the tip is mostly straight, but curves up on one surface, so the dominant stress concentration is at the crack tip identified by the origin. These blurred data points are masked to prevent error propagation.

Table 4.3 presents the RMSD values, experimental data ranges, and NRMSD values for the experimental fields of interest for this small load case. As expected for this case, the data ranges are small. The RMSD values are also small for all of the fields, resulting in reasonably low NRMSD values from 0.023 to 0.069. Good comparison for this case indicates that the experimental method is sensitive enough to consider smaller stress fields that may be useful for high-cycle fatigue testing in materials similar to Homalite-100 or to consider fracture in materials with smaller photoelastic constants than Homalite-100.

As with the analysis previously presented, the photoelastic images are processed first by determination of the isoclinic angle, which requires some manual correction for error due to misalignment of the polarization optics, and then the determination of the isochromatic phase, which is converted to $\sigma_1 - \sigma_2$. Figure 4.50 presents the experimental and theoretical unwrapped isoclinic angle and $\sigma_1 - \sigma_2$ fields, showing good qualitative agreement. The isoclinic angle has the errors common to other isoclinic angle fields previously presented, such as the smoothing of the angle through the region near $\theta = 0$, as shown in Figure 4.50(c). With this small mode-mixity, the isoclinic angle is

Quantity	Units	RMSD (in Units)	Data Range (in Units)	NRMSD (No Units)
α	rad.	0.21	6.69	0.031
$\partial(\sigma_1 + \sigma_2)/\partial x$ from $\lambda/4$ plate method	MPa/mm	0.95	31.1	0.030
$\partial(\sigma_1 + \sigma_2)/\partial y$ from $\lambda/4$ plate method	MPa/mm	0.78	34.5	0.023
$\sigma_1 + \sigma_2$	MPa	0.26	7.18	0.036
$\sigma_1 - \sigma_2$	MPa	0.14	3.89	0.035
σ_1	MPa	0.13	5.14	0.026
σ_2	MPa	0.15	3.74	0.040
σ_{xx}	MPa	0.21	3.91	0.054
σ_{yy}	MPa	0.16	5.26	0.031
σ_{xy}	MPa	0.16	3.73	0.044
σ_{rr}	MPa	0.14	5.39	0.026
$\sigma_{\theta\theta}$	MPa	0.24	3.48	0.069
$\sigma_{r\theta}$	MPa	0.14	3.68	0.038

Table 4.3: Error analysis for various experimental fields for specimen HOMC2 for $K_I = 0.145$ MPa \sqrt{m} and $K_{II} = 0.63$ kPa \sqrt{m}

behaving very close to that of a pure Mode I case, which would have a $\pi/2$ discontinuity at $\theta = 0$ due to the definition of the principal stresses; the larger principal stress changes between the eigenvalues that correspond to the principal stresses when going from $+y$ to $-y$, resulting in a $\pi/2$ change in the angle corresponding to the larger principal stress. This α field has similar RMSD and NRMSD as other presented experimental α fields, indicating consistency of the the error correction methods, regardless of load level. The $\sigma_1 - \sigma_2$ field exhibits the correct shape and almost reaches the same level of stress concentration near the crack tip as the theoretical field, with reasonable NRMSD at 0.035. The higher deviation regions for $\sigma_1 - \sigma_2$ are in front of the crack tip and behind the crack, where the experimental values do not go as low as predicted due to the errors in α in those regions. The wavy nature to the contours is the modulation by the weak interference of the reflected light from the surfaces of the specimen. Since these Fizeau fringes scale up in frequency with increasing thickness (Hecht, 2002), the thicker specimen would experience greater frequency of these weak fringes than the thin specimen for a comparable load. If a heavier Wiener filter (larger window size) had been used on this data, the real photoelastic data may have been obscured. The waviness to

the contours further is one reason for the larger difference between the experimental and theoretical photoelasticity-related fields.

The x and y derivatives of $\sigma_1 + \sigma_2$ and the integrated $\sigma_1 + \sigma_2$ fields from the CGS data are presented in Figure 4.51. The derivatives of $\sigma_1 + \sigma_2$ have some of the lowest NRMSD values, which corroborates the excellent qualitative comparison of the experimental and theoretical fields with the correct shapes and values for most of the field. The region with most difference is at the usual location near the crack tip, where the experimental stress concentration is not high enough. Also, the x derivative field from the vertical shearing phase appears to be elongated in the $-x$ direction behind the crack. The resulting experimental $\sigma_1 + \sigma_2$ in Figure 4.51(f), which no longer includes the constant of integration, has a similar shape to the theoretical field, but the stress concentration is smaller at the crack tip, and the stresses for $-x$ do not curve enough towards the crack tip. These differences are directly due to the previously noted differences in the derivative fields. Even with these errors, the experimental $\sigma_1 + \sigma_2$ has similar NRMSD as the $\sigma_1 - \sigma_2$ field.

The ϵ error related to the derivative assumption for CGS is lower for this case with modest mode-mixity of $\mu_{SIF} = 0.0043$, as indicated in the ϵ error maps in Figure 4.52. Similar to the $K_I = 0.514 \text{ MPa}\sqrt{\text{m}}$ case for HomC1, the largest error is located behind the crack in the vertical shearing direction and around the crack tip for both directions, which is consistent with the noted differences in the derivative fields. Interestingly, even though the CGS interference patterns for this case are closer in density to that of the $K_I = 0.259 \text{ MPa}\sqrt{\text{m}}$ case for HomC1 with its higher mode-mixity of $\mu_{SIF} = 0.058$, the ability of the CGS phases in this case to represent a derivatives of $\sigma_1 + \sigma_2$ is closer to that of the high $K_I = 0.514 \text{ MPa}\sqrt{\text{m}}$ case for HomC1 with its higher $\mu_{SIF} = 0.0085$, demonstrating that the level of mode-mixity has a significant effect on the CGS data. Further quantitative investigation is required to characterize the error involved with using CGS in mixed-mode loading configurations.

The experimental in-plane tensorial stresses all exhibit the same types of good agreement, with a few local problem areas, as the previously discussed cases for HomC1, except the asymmetry in the experimental fields in front of the crack is not as great as in the theoretical fields. In Figure 4.53,

the principal stresses have the correct shapes, but they do not appear to shift toward $-\theta$ as much as the theoretical field. The σ_1 and σ_2 fields have good NRMSD values at 0.026 and 0.40, respectively. In Figure 4.54, the experimental Cartesian stresses presented compare well with theory, except σ_{xx} is more negative for $(-x, +y)$ points and more asymmetric about the x axis than the theoretical case. The experimental polar stresses in Figure 4.55 have the correct shape, but $\sigma_{\theta\theta}$ does not reach the same stress concentration as theory, resulting in a higher NRMSD value of 0.069. Since the experimental $\sigma_{\theta\theta}$ is fairly uniform along the crack and appears to agree well with theory there, the higher error does not appear to have affected the constant of integration calculation, leading to the low error for $\sigma_1 + \sigma_2$.

Figure 4.56 shows two line plots for σ_{yy} along $\theta = 0$. The first shows σ_{yy} versus r , where the theoretical data is within the RMSD bound of the experimental data for $r > 1$ mm, but increases faster than the experimental data near the crack tip. The second figure of the log-log plot of σ_{yy} versus r shows the $-1/2$ slope of the experimental data for larger r , but the slope decreases for smaller r , indicating either a loss of K dominance or large experimental error in this region of σ_{yy} . K dominance near the crack tip is usually lost due to plasticity or 3D stress effects near the crack tip, but plasticity is not likely for this small K_I . The 3D stress effects, which is the breakdown of the basic assumption of plane stress (Rosakis et al., 1990; Krishnaswamy et al., 1991), are the likely culprit for larger error in this field, and the other stress fields, near the crack tip. Since $\sigma_{yy} = \frac{1}{2}(\sigma_1 + \sigma_2) - \frac{1}{2}(\sigma_1 - \sigma_2)\cos(2\alpha)$, all of the errors in $\sigma_1 + \sigma_2$, $\sigma_1 - \sigma_2$, and α conspire near the crack tip to reduce σ_{yy} here. First, the value of $\sigma_1 + \sigma_2$ in front of crack is smaller; second, α is closer to zero than in theory, leading to a larger value of $\cos(2\alpha)$ than in theory; third, $\sigma_1 - \sigma_2$ is slightly larger than theory; and fourth, the combination of a smaller $\sigma_1 + \sigma_2$ with a larger negative $-\frac{1}{2}(\sigma_1 - \sigma_2)\cos(2\alpha)$ results in an under-determination of σ_{yy} as compared to the theoretical plane stress value. This type of error in this line plot prompts checking the $1/\sqrt{r}$ behavior along other values of θ . Unfortunately, this is not a simple matter in the current implementation of the analysis program in MATLAB[®], since the stress fields are represented by a matrix, requiring interpolation of the stress along a line for a given θ . Since the 3D stress effects are confined to near the crack

tip, K dominance can be determined away from the crack tip, as shown in the $1/\sqrt{r}$ behavior for larger r in the σ_{yy} plot. The thicker specimen appears to have greater variation in r behavior along the $\theta = 0$ plane than in the thinner specimen, which is expected given that the 3D effects scale with the thickness of the specimen. The overall smaller σ_{yy} values in the experimental data along the $\theta = 0$ plane in the K -dominant regions in both HomC1 and HomC2 must be due to fields with radial natures on $\theta = 0$, which point to the errors in the isoclinic angle and in $\sigma_1 - \sigma_2$ due to the polarization optic misalignment.

With the overall good comparison of the experimental data with the theoretical data and a few identified errors, this $K_I = 0.145 \text{ MPa}\sqrt{\text{m}}$ load case demonstrates the capability of this experimental method to monitor small K_I cases and also highlights some of improvements that can be made. This K_I is on the order of $K_{Ic}/4$, which is a useful load level for high cycle fatigue testing. The modulation due to the Fizeau interference patterns on top of the photoelastic data needs further mitigation beyond the Wiener filter, such as an anti-reflective coating on the specimen surfaces. Also, the errors due to the rotational misalignment that lead to the local α errors on the crack plane appear to affect the reported behavior of the stresses markedly in this low K_I case, spurring better alignment methods and wrapped α error correction methodologies for Mode I-dominant crack applications.

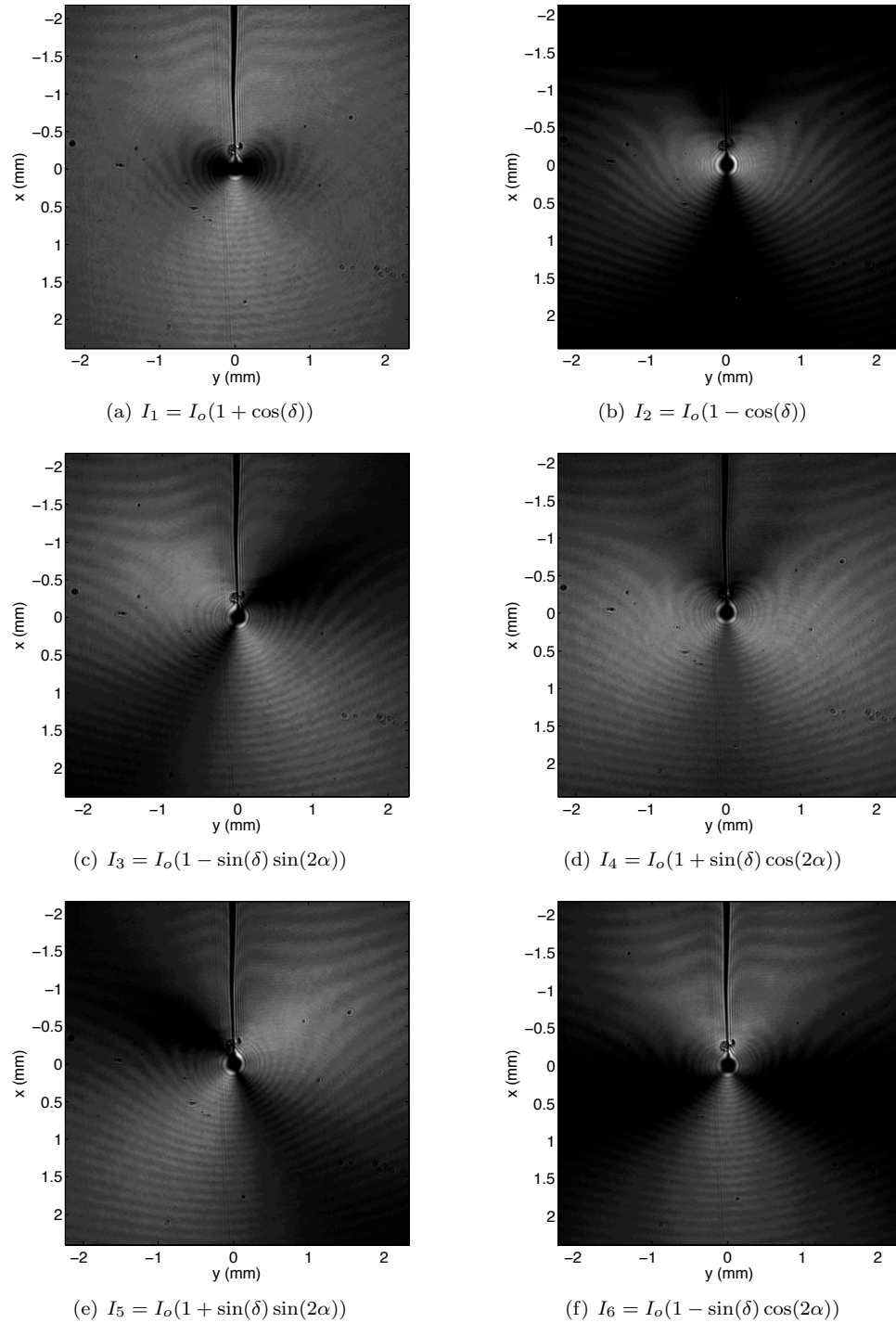


Figure 4.47: Experimental images from six-step phase-shifting photoelasticity for specimen HomC2 for $K_I = 0.145 \text{ MPa}\sqrt{\text{m}}$ and $K_{II} = 0.63 \text{ kPa}\sqrt{\text{m}}$: Caustic shadows obscure the data at the crack tip due to the stress concentration, and the weak high density fringes overlaying the photoelastic fringes are due to the interference of the reflections from the front and back faces of the specimen.

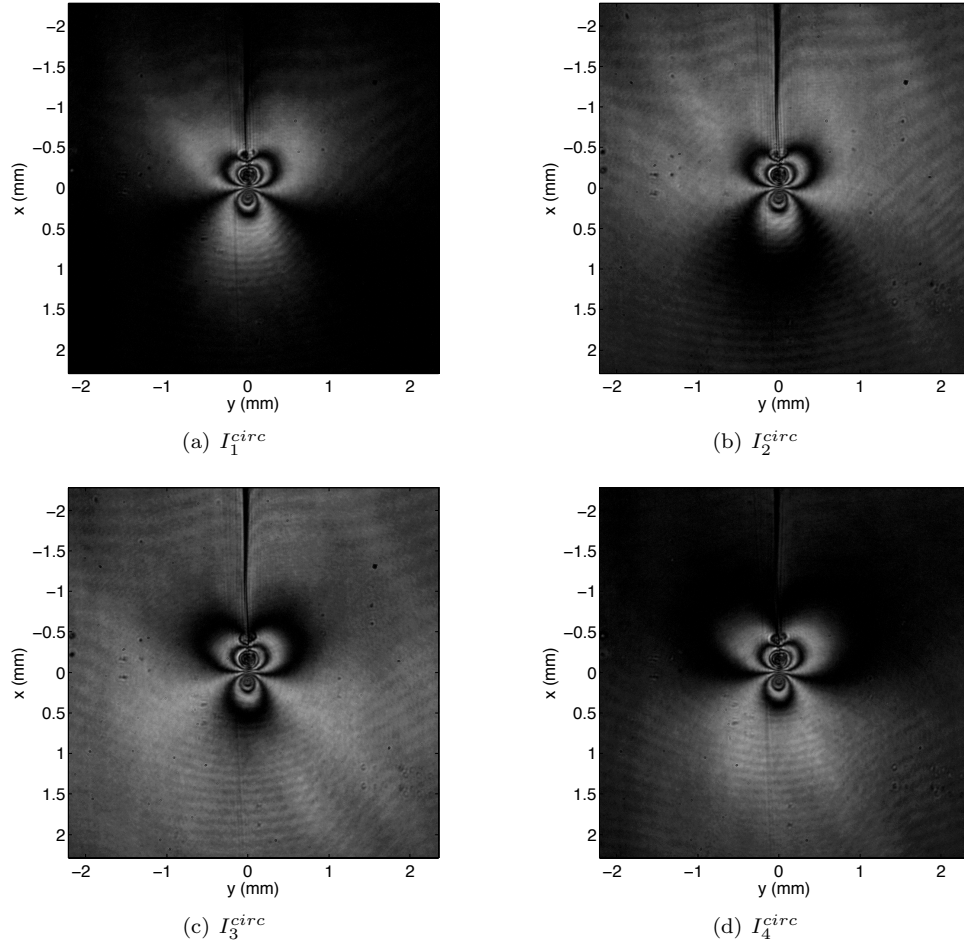


Figure 4.48: Experimental phase-shifted images from vertical shearing CGS using the $\lambda/4$ polarization method for specimen HomC2 for $K_I = 0.145 \text{ MPa}\sqrt{\text{m}}$ and $K_{II} = 0.63 \text{ kPa}\sqrt{\text{m}}$

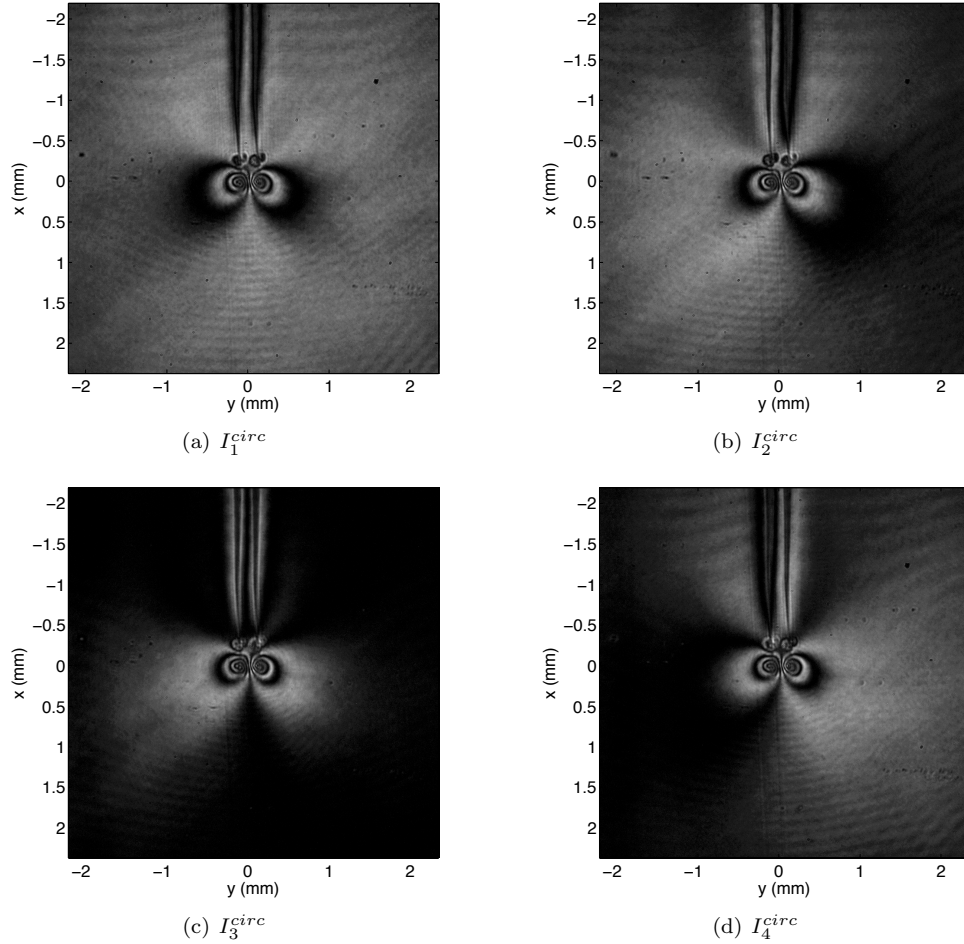


Figure 4.49: Experimental phase-shifted images from horizontal shearing CGS using the $\lambda/4$ polarization method for specimen HomC2 for $K_I = 0.145 \text{ MPa}\sqrt{\text{m}}$ and $K_{II} = 0.63 \text{ kPa}\sqrt{\text{m}}$

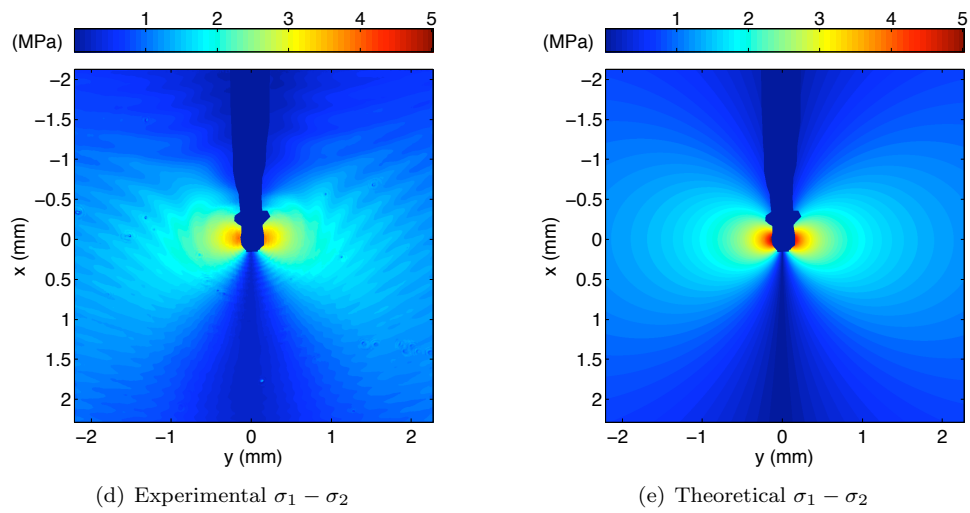
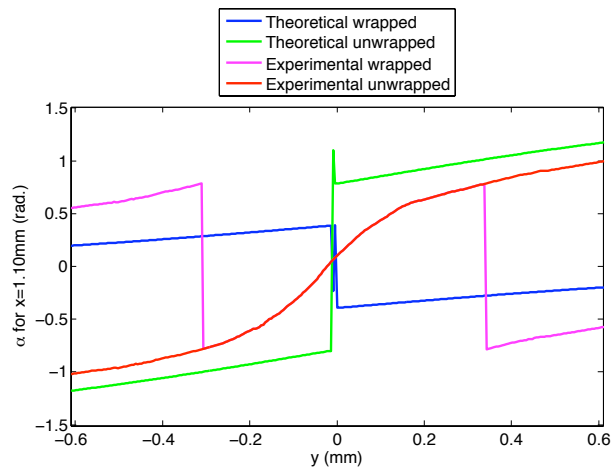
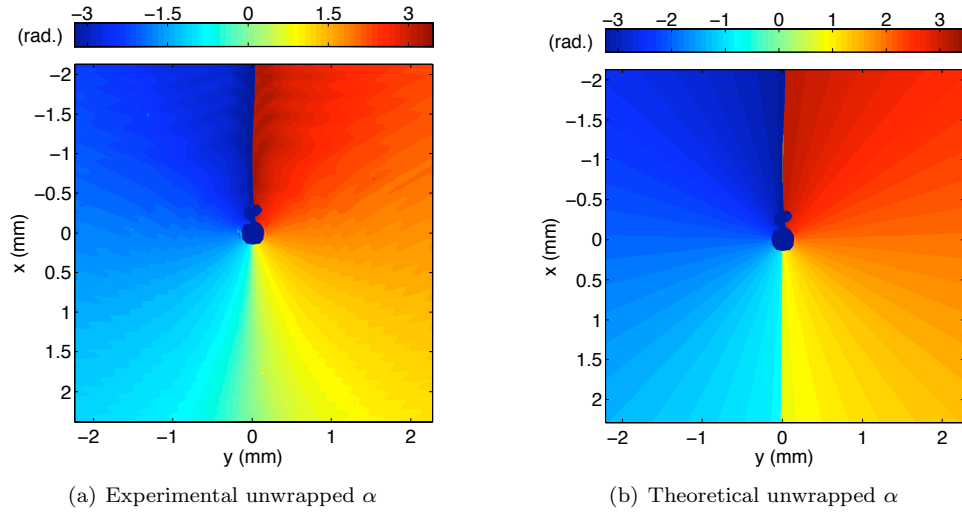


Figure 4.50: Experimental and theoretical unwrapped isoclinic angle with crack region masked in blue and comparison of experimental and theoretical wrapped and unwrapped α for $x = 1.10$